The International Journal of Advanced Manufacturing Technology
https://doi.org/10.1007/s00170-022-09579-1

ORIGINAL ARTICLE

# Microstructural and corrosion effects of HIP and chemically accelerated surface finishing on laser powder bed fusion Alloy 625

**Stephanie Prochaska**[1] · **Owen Hildreth**[2]

Received: 19 April 2022 / Accepted: 20 June 2022


**Abstract**
Hot isostatic pressing (HIP) and surface smoothing are two common post-processing methods to improve the mechanical properties of additively manufactured (AM) laser powder bed fusion (L-PBF) parts. While HIP increases part density and surface smoothing improves fatigue performance, it is unknown how, individually and together, these processes affect a component's corrosion response. This study evaluated the resulting microstructures, surface roughness, and corrosion response of L-PBF Alloy 625 in the as-printed condition and after a standard HIP process to reduce porosity and after chemically accelerated vibratory finishing (CAVF) to improve surface finish. To assess any differences in build orientation, specimens evaluated were printed both vertically (Z-direction) and parallel (XY-direction) to the build platform. None of the specimens pitted during electrochemical evaluation, thus suggesting that the improved corrosion response of the CAVF specimens was due to a reduction in surface area. The Z-oriented as-printed specimen had significantly enhanced corrosion resistance due to a consistent distribution of alloying elements and a densely formed passive layer. Aside from the one exception, the results generally show HIP and CAVF result in minor impacts on the corrosion responses compared to as-printed L-PBF Alloy 625 despite differences in elemental distribution, surface morphology, and microstructural features. These post-processing methods may be employed to improve the mechanical properties of L-PBF Alloy 625 without concern of greatly altering the alloy's inherently good corrosion properties.

**Keywords** Chemically accelerated vibratory finishing · Additive manufacturing · Alloy 625 · Corrosion · Hot isostatic pressing · Microstructure

## 1 Introduction

Compared to conventional techniques, additive manufacturing (AM) has enabled the rapid production of metal parts with complex geometries, less material waste, and the ability to tune microstructures to achieve desired mechanical properties [1]. One metal that has benefited from advances in AM is the nickel-based superalloy Alloy 625 which is utilized in multiple industries for its high-temperature performance, good mechanical properties, and high corrosion resistance [2]. Machining conventional Alloy 625 to achieve desired geometries is, however, very difficult, requiring skilled laborers, slow material removal rates, and overall high costs [3]. While AM is a promising alternative, parts printed through one of the most versatile and common techniques, laser powder bed fusion (L-PBF), are afflicted by internal porosity, undesirable surface conditions, and anisotropic microstructures. These characteristics inherent to the L-PBF process can have deleterious effects on a part's mechanical properties, fatigue performance, and corrosion response [4, 5]. Various post-processing methods including hot isostatic pressing (HIP), heat treatments, and surface smoothing may mitigate the unfavorable as-printed characteristics.

HIP is a common post-processing technique used to reduce internal porosity for improved mechanical performance [6]. In this process, parts are placed in a sealed chamber filled with an inert gas; the chamber is then heated, resulting in an isostatic increase in pressure. For example, common HIP conditions for Ni-based alloys include temperatures ranging from 1120 to 1240 ℃, with pressures between 100 and 160 MPa [5]. As parts soak under these

✉ Owen Hildreth
ohildreth@mines.edu

[1] Materials Science Program, Colorado School of Mines, 1500 Illinois St, Golden, CO 80401, USA

[2] Department of Mechanical Engineering, Colorado School of Mines, 1500 Illinois St, Golden, CO 80401, USA

Published online: 25 June 2022

conditions, plastic deformation collapses internal voids. Creep and diffusion consolidate the part, eliminating any defects while retaining the original geometry [7]. As the temperatures utilized are typically higher than the recrystallization temperature, microstructure refinement from the as-printed condition occurs.

The HIP process does not affect parts' surfaces, and an additional post-process step is often employed to smooth the characteristically rough as-printed surfaces. While many processes such as grinding and machining are largely manual, bulk processes are emerging which are performed across large areas or over entire parts with relatively minimal manual manipulation [8–10]. Chemical-assisted processes are emerging as one subset of bulk methods. Singh et al. utilized chemically assisted magnetic abrasive finishing (CMAF) in removing most Alloy 625 surface irregularities after a 75-min processing time [11]. A self-terminating etching process (STEP) utilized by Lefky et al. removed the top 70 µm of Alloy 718, including print-induced roughness [12]. An STEP formulated for L-PBF 316 L stainless steel reduced the surface roughness by over 50% [13]. Another chemical-based process, chemically accelerated vibratory polishing (CAVF), has been tailored for use on multiple metals to reduce surface roughness [14] and improve the fatigue life of Ti-6Al-4 V [15] and carburized steel [16]. In a corrosion study of multiple chemical and mechanical post-processing techniques on electron-beam powder bed fusion Alloy 718, CAVF resulted in the lowest corrosion current density due to the formation of a Cr-rich passive layer [17]. In CAVF, alloy-specific processing chemistry is applied along with non-abrasive media into a tumbler apparatus with the part. The processing chemistry reacts with the base metal, softening the uppermost layers. The tumbling media removes the softened material layer, and the process repeats until the part achieves the desired surface finish.

While HIP and CAVF can improve part mechanical properties, there has been little evaluation into the effect of these processes on the resulting corrosion response of the treated materials. A part's corrosion response is highly dependent on part composition, microstructure, and surface condition, all of which one or both post-processing methods modify. This work evaluates the individual and combined effects of HIP and CAVF on the resulting material properties of L-PBF Alloy 625 and then evaluates the impact of those properties on the corrosion response. In this way, we can determine if HIP and CAVF maintain Alloy 625's good corrosion resistance and verify that these parts are suitable for use in real-world corrosive environments. Parts printed both vertically and perpendicularly to the build platform underwent HIP, CAVF, or both processes. Additional specimens were evaluated as-printed. Cyclic potentiodynamic polarization characterized the corrosion response, and results showed minor differences between all specimens irrespective of post-processing condition and build orientation. The as-built (AB), non-HIP (NH) Z-oriented specimen had the most favorable corrosion properties due to an even distribution of alloying elements on the surface, promoting a dense passivation layer.

## 2 Materials and methods

### 2.1 Powder characterization

Table 1 gives the chemical composition of the Alloy 625 powder fabricated through vacuum induction melting inert gas atomization by ATI Specialty Materials (New Britain, CT). Powder particles had a D10 of 21.5 µm, D50 of 30.3 µm, and D90 of 42.4 µm. Pursuant to ASTM E2465 [18], X-ray fluorescence (XRF) performed elemental analysis. Combustion/IR detection (CS) and inert gas fusion (GAS), per ASTM E1019 [19], characterized the C, S, O, and N content. Powder chemical composition meets the specification for Alloy 625 alloys [20].

### 2.2 Sample preparation

Standard-sized round axial fatigue test specimens (ASTM E466, [21]) with a gauge length of 16 mm and a gauge length diameter of 8 mm were printed through laser powder bed fusion (L-PBF) at 0 degrees (°) and 90° relative to the build platform on a Concept Laser M2 Dual SLM (GE Additive) printer. Core printing parameters were 370-W laser power and 1200-mm/s scan speed. Outside and inside contour laser powers were 130 W with scan speeds of 225 mm/s. The hatch spacing was 0.11 mm with a 0.06-mm layer thickness. The twelve samples evaluated in this work were 10-mm-long segments, 17 mm in diameter, sectioned from the end of the grip portion of the fatigue test specimens after fatigue testing was performed. Fatigue testing results are documented by Teasley et al. in a separate publication [22]. Since disk samples were sectioned perpendicularly to the build orientation, the XY-direction (horizontal) printed fatigue test specimen generated Z-oriented

**Table 1** Chemical composition of Alloy 625 alloy in wt.% (balance Ni)

| XRF | | | | | | | | | | CS/GAS | | | |
|---|---|---|---|---|---|---|---|---|---|---|---|---|---|
| Mn | Si | P | Cr | Mo | Nb | Co | Ti | Al | Fe | C | S | O | N |
| < 0.01 | < 0.01 | < 0.003 | 22.22 | 8.99 | 3.81 | 0.44 | 0.24 | 0.33 | 0.69 | 0.013 | 0.0007 | 0.0165 | 0.0020 |

sample disks and the Z-direction (vertical) printed fatigue test specimen generated X-oriented sample disks. A schematic depicting the fatigue bar and resulting sample disk orientations is in Supplementary Fig. S1.

A standard HIP (1120–1240 ℃, 100–165 MPa, 3–4 h, furnace cooled) [5] processed four samples (two of each build orientation). All HIP and NH samples were subsequently recrystallized in a vacuum atmosphere at 1038 ℃ for 80 min [23].

One as-built (AB) and HIP sample of each build orientation underwent the REM Surface Engineering (Brenham, Texas) Extreme Isotropic Superfinishing (ISF®) process. In this patented chemically accelerated vibratory finishing (CAVF) process, chemical polishing first removes macro surface defects. The proprietary chemistry forms a brittle self-assembled monolayer on the substrate which is mechanically removed with abrasive media in a tumbler-type apparatus. With the continual addition of the chemistry and reformation of the surface monolayer, surface protrusions are gradually smoothed, and the surface is eventually planarized. In a final step, the monolayer is removed from the surface with detergent. Table 2 gives sample identification and processing conditions for all samples utilized in this study.

### 2.3 Characterization and electrochemistry

Six 5600-µm-long scans with a lateral resolution of 0.062 µm performed with a Bruker DektakXT contact profilometer characterized the surface roughness of each disk. The stylus was 2 µm with a 3-mg load. Data was filtered through a Gaussian regression short cutoff ($\lambda_s$) at 2.5 µm and a long cutoff ($\lambda_c$) at 0.8 mm [24]. X-ray diffraction (XRD) was performed with a Bruker AXS D2 Phaser diffractometer with a Co Kα source and two-theta from 27 to 130°. Relative crystallite size, τ, was determined through the Scherrer equation, $\tau = \frac{K\lambda}{\beta cos\theta}$. The shape factor, $K$, is 0.94; the x-ray wavelength, λ, is 1.79 angstroms; β is the full-width half maximum of the diffraction peaks; and θ is the Bragg diffraction angle [25].

An LECO MSX205 sectioning machine cross-sectioned the specimens, and they were subsequently cold mounted in epoxy (EpoFix, Struers). Samples were sequentially ground with silicon carbide paper (LECO) and polished with diamond LECO suspensions to a one-micron finish. The polished metallography specimens were stain etched for 40 s with acetic glyceregia (1:2:3 parts nitric acid, acetic acid, and hydrochloric acid, respectively, with two drops of glycerol) to reveal the grain boundaries. A Zeiss Axio Vert.A1 inverted microscope imaged the microstructures. Surface morphology was evaluated with a SEMTech Solutions Model 3300 Field Emission Scanning Electron Microscope (SEM) at an accelerating voltage of 20 kV and a 23-mm working distance. A WIN10 ™ Energy Disperson Spectrometer (EDS) operating at 20 kV assessed the elemental composition.

Potentiodynamic polarization was performed in a 0.6-M sodium chloride (NaCl, 3.5 wt.% Fischer) in deionized water (18 MΩ, Thermo Scientific Smart2Pure 3 UV/UF) solution at room temperature using a Princeton Applied Research Parstat MC potentiostat. The standard three-electrode cell consisted of the sample working electrode, 6.35-mm-diameter graphite rod counter electrode, and a silver/silver chloride (Ag/AgCl) reference electrode ionically connected through a 4-M potassium chloride (KCl) salt bridge. Exposing the specimen to the electrolyte for 48 h prior to polarization testing achieved a stable open circuit potential. Cyclic polarization plots (CPP) were generated by scanning from 1 V more negative than the open circuit potential (OCP) to a vertex of 1.5 V more positive than the OCP at a rate of 10 mV/s. Corrosion potential ($E_{corr}$), passivation potential ($E_{pass}$), and passive current density ($i_{pass}$) were determined through analysis of the resulting polarization curves. All recorded potentials are reported relative to a standard hydrogen electrode (SHE) after shifting the recorded Ag/AgCl values by + 0.197 V.

**Table 2** Specimen IDs, build orientations, and processing conditions

| Specimen ID | Build orientation | HIP method | Surface finishing |
|---|---|---|---|
| NH AB X | X/Y | N/A | As-built |
| NH AB Z | Z | N/A | As-built |
| NH CAVF X | X/Y | N/A | CAVF |
| NH CAVF Z | Z | N/A | CAVF |
| HIP AB X | X/Y | Standard | As-built |
| HIP AB Z | Z | Standard | As-built |
| HIP CAVF X | X/Y | Standard | CAVF |
| HIP CAVF Z | Z | Standard | CAVF |

## 3 Results and discussion

A metal's electrochemical response is dependent on more than one property and can differ when parameters such as chemical composition, surface roughness, and microstructure are varied. Since all specimens were produced with the same powder having uniform chemistry, chemical composition's impact on corrosion properties was not considered as part of this work. Furthermore, XRD results, presented in Supplementary Fig. S2, show Alloy 625 characteristic diffraction patterns for all evaluated specimens [26]. Differences in peak intensities between all specimens were negligible, thus indicating no phase changes occurred during HIP

that were not subsequently resolved through annealing. Furthermore, the CAVF process did not impart any near-surface phase transformations; however, due to surface smoothing, the diffraction peaks for the CAVF specimens are less noisy than those of the specimens with the as-built surfaces.

HIP elicits a microstructural change, and CAVF modifies a part's surface morphology, so we studied the effect on corrosion response of both processing parameters individually. To assess the role of the microstructure without the influence of surface features, we evaluated the CAVF specimens in the NH and HIP conditions. We assessed the specimens with AB surfaces to subsequently evaluate the effect of surface features on corrosion properties. Finally, we discuss the combined effects of HIP and CAVF on the properties of L-PBF Alloy 625.

### 3.1 Surface roughness

Corrosion concentration cells may form in or around the crevices inherent in rough surfaces, negatively impacting a part's corrosion resistance. Extremely limited work exists on the effect of surface roughness on the corrosion response of Alloy 625, with none addressing the impacts of diminutive roughness differences [27]. For other austenitic material systems such as 316L stainless steel, surface roughness has a negligible effect on corrosion response once Ra decreases below 0.5 µm [28, 29]. Figure 1 shows the Ra surface roughness of the CAVF specimens. For X-oriented (parallel) samples, Ra surface roughness was $0.16 \pm 0.05$ µm for NH and $0.34 \pm 0.08$ µm for HIP. The surface roughness of the Z-oriented samples was $0.32 \pm 0.13$ µm for NH and $0.12 \pm 0.03$ µm for HIP. For NH specimens, the X-oriented specimens had lower roughness values than the Z-oriented specimens. Contrarily, the X-oriented HIP specimen had a significantly rougher surface than the Z-oriented (perpendicular) specimen. However, the differences in roughness between all CAVF specimens are very small with an overall standard deviation of 0.11 µm across 24 individual measurements. As a stepwise process, multiple CAVF cycles can produce the desired roughness. The surface roughness obtained for the CAVF specimens in this work are negligible, and thus, microstructure and alloying element distribution dominates the electrochemical behavior of the CAVF specimens.

Figure 2 shows the Ra surface roughness of the as-built L-PBF Alloy 625 specimens. For samples oriented in the X-direction, the surface roughness was $2.79 \pm 0.91$ µm for NH and $2.23 \pm 0.32$ µm for HIP. The surface roughness of the Z-oriented samples was $7.0 \pm 1.2$ µm for NH and $6.4 \pm 1.6$ µm for HIP. Congruent to previous studies on the surface roughness of L-PBF Alloy 625, the Z-oriented surfaces were significantly rougher than the X-oriented surfaces [30]. These differences are attributed to balling effects and partially melted powders on the surface which are more often resolved in X-oriented samples by remelting during subsequent laser passes [31]. The standard HIP had an insignificant effect on surface roughness compared to the NH specimens. Since the HIP AB X specimen had a smoother surface than the NH AB X specimen, but the NH AB Z specimen had a smoother surface than the HIP AB Z specimen, there is no significant effect of HIP on surface roughness. HIP is known to typically not impact the surface roughness of AM metals [32]. Supplementary Fig. S3 shows the plots for the average maximum peak to valley roughness (Rz), the maximum profile valley depth (Rv), and the skewness (Rsk).

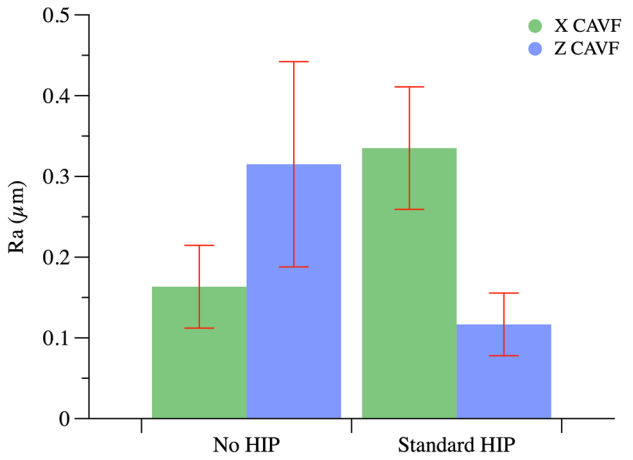


**Fig. 1** Ra surface roughness for all CAVF specimens evaluated. For NH, the Z-orientation resulted in rougher surfaces than the X-orientation. The X-oriented HIP specimen had a rougher surface than the Z-specimen. Generally, all roughness values are so small that they are considered insignificant to corrosion response

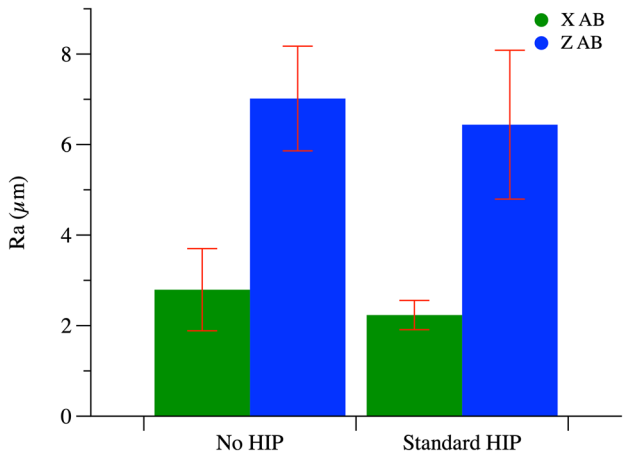


**Fig. 2** Ra surface roughness for all as-built specimens evaluated. For NH and HIP specimens, the Z-orientation exhibited rougher surfaces than the X-orientation

### 3.2 Microstructure

The microstructure of Alloy 625 depends on annealing temperature and time, resulting in variation of phases, grain size and shape, precipitates, and dislocation density—all features which may impact the corrosion response. Understanding the microstructure evolution aids in selecting the appropriate heat treatment scheme for the desired material properties. Precipitation hardening involving the metastable body-centered tetragonal γ" [$Ni_3$(Nb, Al, Ti)] occurs between 550 and 650 ℃, with intermetallics and carbides possible up to 750 ℃ [33]. Through prolonged aging above 750 ℃, γ" dissolves into the orthorhombic δ-phase. Carbides of the type $M_{23}C_6$, $M_6C$, and MC can form between 760 and 980 ℃. Solution annealing at temperatures of approximately 1093 ℃ dissolves most precipitates except for large NbC. L-PBF Alloy 625 microstructures also vary from the as-printed condition with several heat treatment times and temperatures and with HIP. Marchese et al. showed an evolution in microstructure from the AB state's characteristic melt pools and epitaxial columnar grains to an equiaxed microstructure containing fine 10-μm grains to coarser 90-μm grains and twin boundaries [34]. In a study of heat treatment and HIP on the microstructure of L-PBF Alloy 625, Kreitcberg et al. showed that standard HIP results in equiaxed grains averaging 40–50 μm [5].

Since all as-printed and HIP specimens evaluated in this work underwent the same post-processing heat treatment, the resulting microstructures are very similar despite build orientation and HIP methods. Furthermore, the CAVF process is low temperature and does not impart any bulk microstructural changes [35]. Figure 3 shows the cross-sectional micrographs of the NH and HIP Alloy 625 specimens built in the X- and Z-orientations. The consistent heat treatment produced no major microstructural differences between HIP and NH samples, with all microstructures having fine-to-coarse equiaxed grains from approximately 5 to 100 μm in size. However, the HIP microstructures show more annealing twins compared to the NH specimens. Annealing twins form in conventional Alloy 625 when the microstructure attempts to resolve residual stresses imparted through the application of heat and mechanical forces [36, 37]. In austenitic materials, twins suppress Cr depletion and improve resistance to intergranular corrosion [38, 39].

All micrographs show the formation of dark, sometimes coarse precipitates. Hyer et al. identified these precipitates as MC carbides of type (Ti, Nb, Mo, Ni, Cr, Fe)C which form in L-PBF Alloy 625 after annealing at temperatures above approximately 1000 ℃ [40]. Dubiel and Sieniawski found mainly NbC carbides [41]. As described later in this section and in "Electrochemistry," NbC can improve corrosion resistance. The near-surface micrographs in Fig. 4 show these coarse (primary) and fine carbides in the NH

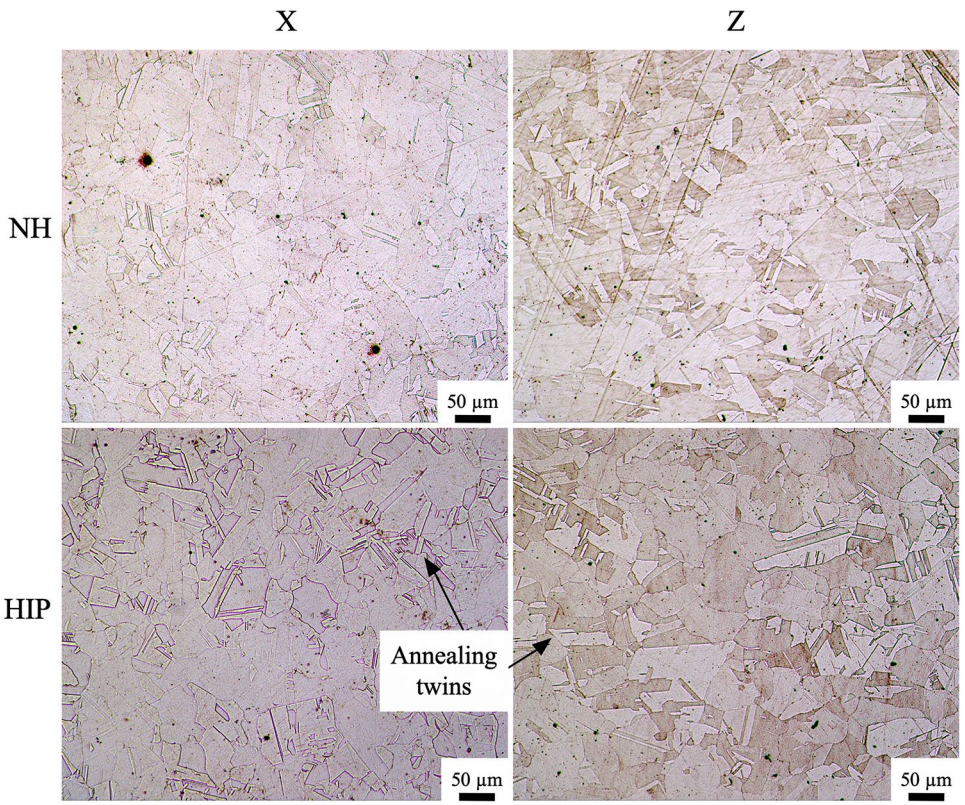


**Fig. 3** Cross-sectional micrographs of the NH and HIP specimens showing very similar microstructures. HIP specimens had more annealing twins than the NH specimens. No differences were observed between the X- and Z-build orientations

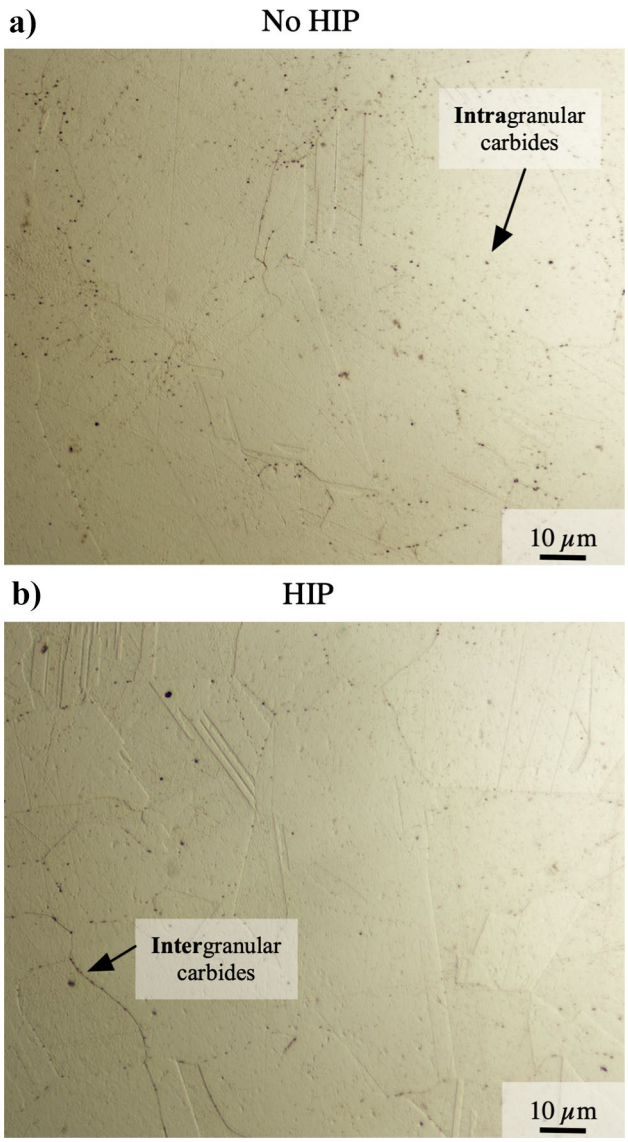


**Fig. 4** Near-surface micrographs showing the carbides in **a** the NH X specimen and **b** the HIP X specimen. Carbides in the HIP specimen were mostly intergranular, while the NH specimen's single anneal did not allow for significant diffusion or coarsening out of the matrix

and HIP specimens. Previous studies have also noted the formation of various-sized MC carbides in Alloy 625 after solution annealing [34]. The NH micrograph shows markedly more intra- and intergranular carbides than the HIP micrograph. Additionally, the carbides in the HIP specimens appear mostly intergranular. Although undocumented in the current literature on L-PBF Alloy 625, a possible explanation for the differences in carbide segregation in the two samples could be a result of the HIP specimens undergoing two separate anneals. During the HIP process itself, carbide precipitates nucleated at grain boundaries as well as near dislocations [42]. Upon subsequent solution annealing, the already-formed precipitates coarsened and diffused toward grain boundary regions and out of the matrix [43]. In contrast, the single solution anneal of the NH specimens precipitated carbides throughout the matrix but did not allow enough time for grain boundary diffusion of significant coarsening. De Terris et al. have investigated the recrystallization speed of L-PBF Alloy 625 with varying levels of energy (dislocation) densities [44]. Their work found that recrystallization during solution annealing occurred more rapidly in specimens with higher starting dislocation densities. Therefore, it is not improbable that other mechanisms, such as precipitation kinetics, could also differ for materials with varying energies subject to the same processing conditions.

Surface morphology was also similar for HIP and NH specimens of each build orientation. Figure 5 shows the EDS analysis results for the as-printed NH and HIP specimens. The 500 × SEM images for the X-oriented specimens show significant surface undulation with evidence of remelting. The Z-oriented specimen surfaces are relatively flat and covered with unsintered particles. Varying severity of cracking is also visible, with the NH AB Z specimen having mainly dispersed pore-like features while the pits connect to form long cracks on the HIP AB Z surface. These observations are consistent with the surface roughness findings. The 15–20-μm diameter powder particles of the Z-specimens result in rougher surfaces on average than the comparatively smooth X-oriented specimens which are devoid of major surface features.

The elemental distributions across the X-oriented specimens are notably different, particularly regarding Cr and Nb. To an extent, O atomic concentration trends with Cr for both X-oriented specimens, indicating chromium oxide formation. The NH AB X specimen's Cr and Nb atomic concentrations both fluctuate near 20 percent, with a few spikes above 60 percent for Cr and influxes toward 30 percent for Nb. The HIP AB X surface, however, is enriched with Cr—at multiple locations across the line scan Cr atomic concentrations exceed 80 percent, with an average concentration nearing 40 percent. This enhancement suggests significant, detrimental Cr depletion elsewhere. For both X- and Z-oriented HIP specimens, Nb is frequently depleted across the line scans, whereas the NH specimen line scans show a continuous concentration rarely reaching zero. Interdendritic elemental segregation of Nb in has been previously observed for L-PBF Alloy 625, but mainly in as-printed alloys subject to rapid solidification [27, 45].

Across unsintered powder particles, both Z-oriented specimen line scans reveal large spikes in Cr and O atomic concentrations. Generally, Cr across specimen NH AB Z averages near the powder's starting atomic concentration of approximately 22 percent, while Nb concentration fluctuates around about 10 percent. The influx of Nb is likely due to

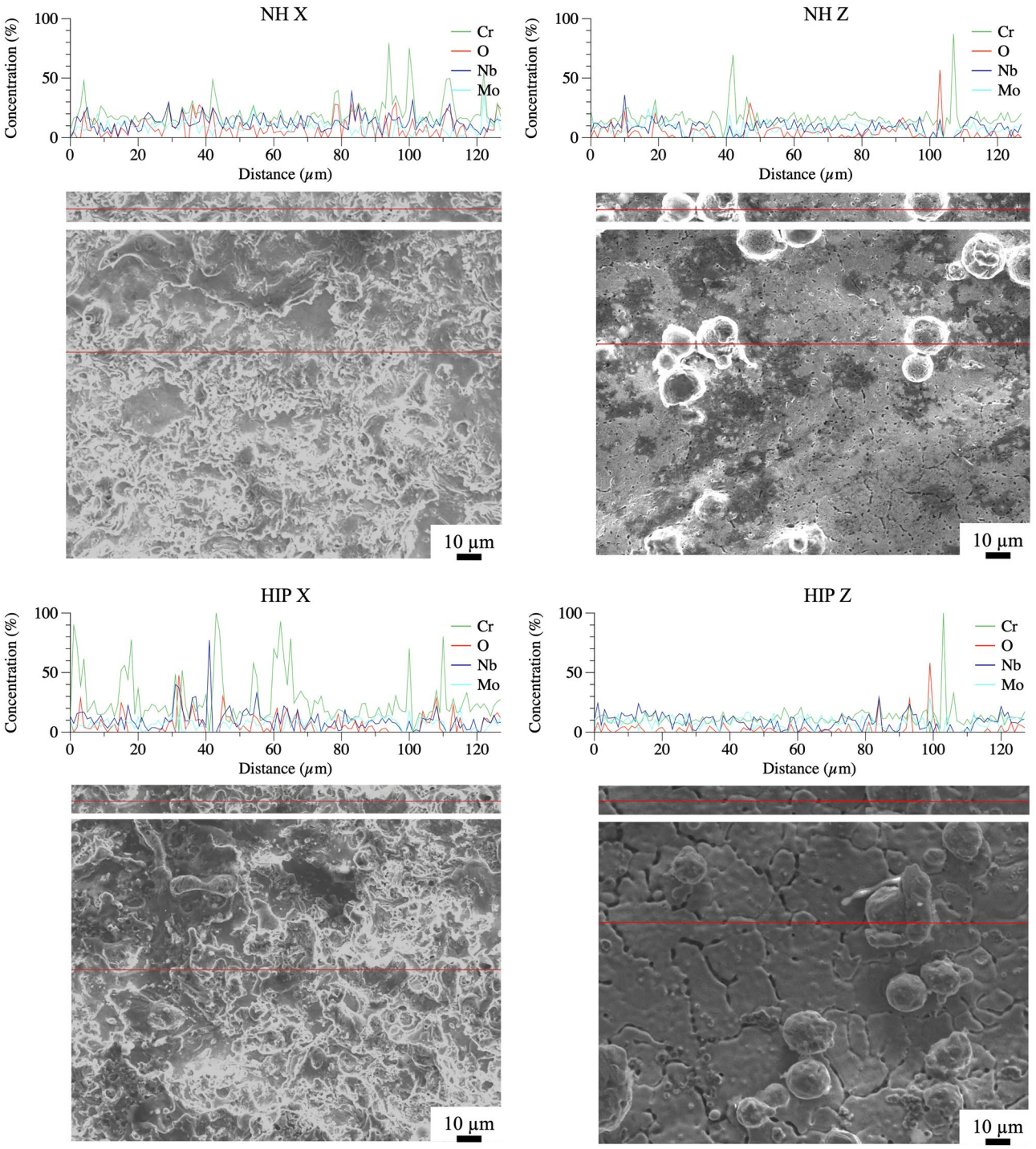


**Fig. 5** SEM and EDS results showing the surface morphologies of the X- and Z-oriented as-printed NH and HIP specimens. Surface morphologies differ significantly with build orientation

the previously discussed retention and relative homogeneous distribution of MC in the form of NbC precipitates after solution annealing. Due to carbon's low atomic mass and EDS quantification limitations, this work did not measure C content. Previous work has found improved pitting resistance in wrought Alloy 625 containing NbC due to the decreased availability of C to form carbides with Cr [46]. Conversely, the average Cr atomic concentration of the HIP AB Z specimen is notably less than 20 percent, frequently dipping below or matching the concentration of Nb. In addition to

Cr, Mo is added to Alloy 625 and other austenitic metals as an alloying element and improves corrosion resistance by increasing the passive film effectiveness and reducing pitting [47]. Relatively consistent distribution of Mo is noted for all specimens evaluated, with only minor deviations among specimen types. The surface morphologies and elemental distribution of all CAVF specimens are unremarkable with a similar, even distribution of alloying elements across the surfaces regardless of specimen type. EDS map scans of CAVF specimens are in Supplementary Fig. S4.

### 3.3 Electrochemistry

The CPP curves showing the forward sweep of the NH and HIP specimens are in Supplementary Fig. S5, which also shows the curves including the reverse sweep. In the figures, CAVF curves are indicated by dashed lines. Figure 6 graphically depicts the corrosion properties extracted from evaluating the CPP curves, and Supplementary Table S1 provides the extracted values. $E_{corr}$, the potential at which the current density is the smallest, denotes the corrosion potential—more positive values indicate better corrosion resistance. $E_{pass}$ and $i_{pass}$ are the potential and current density at the inflection point where current density becomes relatively stable and unchanging. $E_{pass}$ is the protection potential, or potential at which the stable passivation layer forms. $i_{pass}$ relates to the density of the passivation layer, with smaller values indicating inhibited current flow and thus a denser and more protective passive layer. All CPP curves show positive hysteresis loops in the reverse sweep, therefore signifying no pitting occurred in the samples over the applied potential range and breakdown potentials were not reached. The pitting resistance of Alloy 625 is attributed to the high Ni content, and a lack of pit formation has been previously noted for L-PBF Alloy 625 exposed to various corrosive media [27, 48].

In the absence of surface effects, the electrochemical behaviors of the L-PBF Alloy 625 CAVF specimens are dominated by the microstructures. From Fig. 6c, $i_{pass}$ decreases when Alloy 625 undergoes HIP. This trend is noted for both X- and Z-oriented CAVF specimens. $E_{corr}$ trends with $i_{pass}$, with $E_{corr}$ becoming slightly more positive from NH CAVF (X: − 0.70 $V_{SHE}$, Z: − 0.71 $V_{SHE}$) to HIP CAVF (X: − 0.68 $V_{SHE}$, Z: − 0.67 $V_{SHE}$). Cabrini et al. have shown that for L-PBF Alloy 625 subject to high cooling rates, there is an oversaturation and more even distribution of alloying specimens throughout the matrix rendering them more available to form dense passive layers [48]. Furthermore, smaller grain sizes and dislocations enhance the distribution since the grain boundaries and dislocations function as express routes for passivating species to and from the surface, providing additional strength and stability to the passive film [49, 50]. Since grain sizes were similar for NH and HIP specimens, the enhancement in the passive layer of the HIP specimens is most likely due to the increased dislocation density imparted through the HIP process and the annealing twins reducing the incidence of intergranular corrosion. Ultimately, the differences in $E_{corr}$ of the CAVF specimens are largely insignificant for practical purposes.

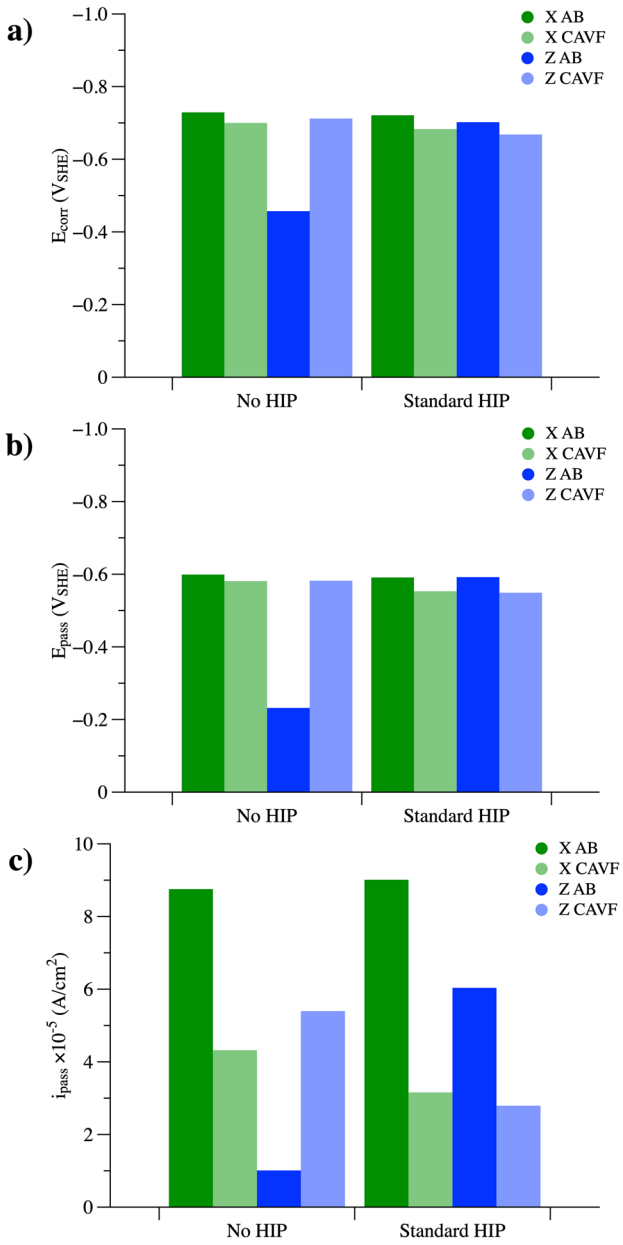


**Fig. 6** (**a**) $E_{corr}$, (**b**) $E_{pass}$, and (**c**) $i_{pass}$ values extracted from the CPP plots for all specimens evaluated in this work. Generally, all specimens had very similar corrosion properties despite different processing conditions. The NH AB Z specimen had significantly lower corrosion density and thus a higher corrosion potential than all of the other specimens

As with the CAVF specimens, $E_{corr}$ of the AB surfaces directly relates to passive film density. $i_{pass}$ decreases

with increasing average surface roughness for the AB Z specimens, which is an unexpected result since rougher surfaces typically afford poorer corrosion properties due to the propensity for crevice corrosion and a defective passive layer in the rougher surfaces [27]. However, the lack of pitting potential suggests that crevice corrosion did not occur in any of the specimens and surface roughness did not play a role in the corrosion mechanism. Both X-oriented NH and HIP specimens have relatively similar surface morphologies despite processing conditions, and consequently, $i_{pass}$ and $E_{corr}$ are also remarkably similar for these specimens. Elemental analysis suggested the segregation of Cr to the surfaces of the X-oriented specimens, resulting in decreased corrosion resistance compared to the Z-oriented specimens. The NH Z AB specimen had significantly better corrosion properties than all of the other specimens evaluated in this work due to the consistent and slightly enriched Cr distribution. Compared to the HIP AB Z specimen which had cohesive pits forming long crack-like features which destabilized the passive layer, the NH specimen's surface pits were significantly smaller and not connected, thus enabling the formation of a dense and stable passive film and resulting in superior corrosion resistance. The improvement in corrosion behavior of the NH AB Z specimen is also due to the more even distribution of MC carbides across the specimen surfaces instead of segregation in the grain boundaries as in the HIP specimen. Seifert et al. have shown that NbC carbides improve corrosion resistance due to niobium's affinity for carbon, thus impeding the formation of deleterious chromium carbides [51].

Compared to the AB surfaces, CAVF appeared to improve the corrosion resistance of Alloy 625. Since none of the specimens pitted during electrochemical evaluation, we assume that the difference is due to surface area effects, with the AB specimens having much higher surface areas than the CAVF specimens, thus resulting in a current density increase and corrosion potential decrease. Increases in near-surface dislocation density also explain the CAVF specimens' better corrosion response. By their nature, mechanical deformation processes such as CAVF increase the near-surface dislocation density within a part which improves alloying element migration and distribution. Wu et al. found a significant increase in residual compressive stress depth and increased dislocation density of a shot-peened Alloy 625 surface [52]. As alluded to previously, chromium has been shown to use these dislocations as shortcuts to diffuse to the surface which promotes and enriches passive film formation [48]. While this work did not focus on quantifying the dislocation density of each specimen, relative dislocation density was roughly estimated by the Scherrer equation, through which $\frac{1}{\tau^2}$ is subsequently dislocation density [53, 54]. This cursory analysis found the CAVF specimens to have much higher relative dislocation densities compared to the AB counterparts.

## 4 Conclusions

This work evaluated the microstructural, morphological, and electrochemical changes elicited in L-PBF Alloy 625 having undergone no processing, HIP, and/or CAVF. While HIP had a mixed effect on corrosion response depending on build orientation, the benefits to mechanical properties likely outweigh any detrimental corrosion effect. Additionally, CAVF improved the corrosion potential of every specimen evaluated except NH AB Z. The combined effect of both processes resulted in the most desirable corrosion properties; however, the improvement from CAVF was less than 100 $mV_{SHE}$. The following generalizes the main findings of this work.

- The NH and non-CAVF control specimens (NH AB X and NH AB Z) formed equiaxed grains after solution annealing with a homogeneous distribution of MC, likely NbC, carbides across the matrix. The NH AB Z specimen had the most dense, coherent passive film and most positive corrosion potential of all specimens evaluated.
- The HIP and non-CAVF specimens exhibited significant cracking across the surface, possibly caused by carbide segregation to the grain boundaries, which destabilized the passivation layer and reduced the corrosion resistance compared to NH specimens.
- CAVF increased the dislocation density in all processed specimens. Coupled with the effect from surface area reduction, CAVF specimens had better corrosion properties than non-CAVF.
- Generally, the impact of HIP and CAVF post-processing on the corrosion response of L-PBF Alloy 625 is minimal. Considerations of resulting corrosion response may not be necessary when processing this material with one or both of these methods.

**Abbreviations** AB: As-built; AM: Additive manufacturing; CAVF: Chemically accelerated vibratory finishing; CMAF: Chemically assisted magnetic abrasive finishing; CPP: Cyclic potentiodynamic polarization; CS: Combustion/IR detection; $E_{corr}$: Corrosion potential; EDS: Energy-dispersive X-ray spectroscopy; $E_{corr}$: Passivation potential; GAS: Inert gas fusion; HIP: Hot isostatic pressing; $i_{pass}$: Passivation current; ISF: Isotropic superfinishing; L-PBF: Laser powder bed fusion; NH: Non-HIP; OCP: Open circuit potential; SEM: Scanning electron microscope; SHE: Standard hydrogen electrode; STEP: Self-terminating etching process; XRF: X-ray fluorescence; XRD: X-ray diffraction

**Supplementary information** The online version contains supplementary material available at https://doi.org/10.1007/s00170-022-09579-1.

**Acknowledgements** The authors acknowledge the National Science Foundation for their generous financial support (NSF CAREER: 1944516). The authors would also like to thank and acknowledge REM Surface Engineering for performing the ISF® process on the specimens used in this work.

**Author contribution** All authors contributed to the study's conception and design. Material preparation, data collection, and analysis were performed by Stephanie Prochaska. The first draft of the manuscript was written by Stephanie Prochaska, and all authors commented on previous versions of the manuscript. All authors read and approved the final manuscript. Funding resources and supervision were provided by Prof. Owen Hildreth.

**Funding** This material is based upon work supported by the National Science Foundation under Grant No. CAREER 1944516.

## Declarations

**Competing interests** The authors declare no competing interests.

## References

1. Milewski JO (2017) Envision. In: Additive manufacturing of metals, Springer International Publishing, Cham: 1–6. https://doi.org/10.1007/978-3-319-58205-4_1
2. Tian Z, Zhang C, Wang D, Liu W, Fang X, Wellmann D, Zhao Y, Tian Y (2019) A review on laser powder bed fusion of Inconel 625 nickel-based alloy. Appl Sci 10:81. https://doi.org/10.3390/app10010081
3. Parida AK, Maity K (2018) Comparison the machinability of Inconel 718, Inconel 625 and Monel 400 in hot turning operation. Eng Sci Technol Int J 21:364–370. https://doi.org/10.1016/j.jestch.2018.03.018
4. Gonzalez JA, Mireles J, Stafford SW, Perez MA, Terrazas CA, Wicker RB (2019) Characterization of Inconel 625 fabricated using powder-bed-based additive manufacturing technologies. J Mater Process Technol 264:200–210. https://doi.org/10.1016/j.jmatprotec.2018.08.031
5. Kreitcberg A, Brailovski V, Turenne S (2017) Effect of heat treatment and hot isostatic pressing on the microstructure and mechanical properties of Inconel 625 alloy processed by laser powder bed fusion. Mater Sci Eng A 689:1–10. https://doi.org/10.1016/j.msea.2017.02.038
6. A01 Committee, Practice for hot isostatic pressing of steel, stainless steel, and related alloy castings, ASTM International n.d. https://doi.org/10.1520/A1080_A1080M-19
7. Radomir I, Geamăn V, Stoicănescu M (2012) Densification mechanisms made during creep techniques applied to the hot isostatic pressing, Procedia - Soc. Behav Sci 62:779–782. https://doi.org/10.1016/j.sbspro.2012.09.131
8. Sun Y, Bailey R, Moroz A (2019) Surface finish and properties enhancement of selective laser melted 316L stainless steel by surface mechanical attrition treatment. Surf Coat Technol 378:124993. https://doi.org/10.1016/j.surfcoat.2019.124993
9. Mesicek J, Ma Q-P, Hajnys J, Zelinka J, Pagac M, Petru J, Mizera O (2021) Abrasive surface finishing on SLM 316L parts fabricated with recycled powder. Appl Sci 11:2869. https://doi.org/10.3390/app11062869
10. Walczak M, Szala M (2021) Effect of shot peening on the surface properties, corrosion and wear performance of 17–4PH steel produced by DMLS additive manufacturing. Arch Civ Mech Eng 21:157. https://doi.org/10.1007/s43452-021-00306-3
11. Singh G, Kumar H, Kansal HK, Srivastava A (2020) Effects of chemically assisted magnetic abrasive finishing process parameters on material removal of Inconel 625 tubes. Procedia Manuf 48:466–473. https://doi.org/10.1016/j.promfg.2020.05.070
12. Lefky CS, Gallmeyer TG, Moorthy S, Stebner A, Hildreth OJ (2019) Microstructure and corrosion properties of sensitized laser powder bed fusion printed Inconel 718 to dissolve support structures in a self-terminating manner. Addit Manuf 27:526–532. https://doi.org/10.1016/j.addma.2019.03.020
13. Hoffman R, Hinnebusch S, Raikar S, To AC, Hildreth OJ (2020) Support thickness, pitch, and applied bias effects on the carbide formation, surface roughness, and material removal of additively manufactured 316 L stainless steel. JOM. https://doi.org/10.1007/s11837-020-04422-y
14. Atzeni E, Balestrucci A, Catalano AR, Iuliano L, Priarone PC, Salmi A, Settineri L (2020) Performance assessment of a vibro-finishing technology for additively manufactured components. Procedia CIRP 88:427–432. https://doi.org/10.1016/j.procir.2020.05.074
15. Witkin DB, Patel DN, Helvajian H, Steffeney L, Diaz A (2019) Surface treatment of powder-bed fusion additive manufactured metals for improved fatigue life. J Mater Eng Perform 28:681–692. https://doi.org/10.1007/s11665-018-3732-9
16. Winkelmann L, Michaud M, Sroka G, Swiglo AA (2002) Impact of isotropic superfinishing on contact and bending fatigue of carburized steel. Adv Surf Eng SAE International, Las Vegas p. 13
17. Sadeghi M, Diaz A, McFadden P, Sadeghi E (2022) Chemical and mechanical post-processing of Alloy 718 built via electron beam-powder bed fusion: Surface texture and corrosion behavior. Mater Des 214:110405. https://doi.org/10.1016/j.matdes.2022.110405
18. E01 Committee, Test method for analysis of Ni-base alloys by wavelength dispersive X-ray fluorescence spectrometry, ASTM International n.d. https://doi.org/10.1520/E2465-19
19. E01 Committee, Test methods for determination of carbon, sulfur, nitrogen, and oxygen in steel, iron, nickel, and cobalt alloys by various combustion and fusion techniques, ASTM International, n.d. https://doi.org/10.1520/E1019-08
20. AMS F Corrosion Heat Resistant Alloys Committee, Nickel alloy, corrosion and heat-resistant, sheet, strip, and plate, 62Ni - 21.5Cr - 9.0Mo - 3.7 Cb (Nb), Solution Heat Treated, SAE International n.d. https://doi.org/10.4271/AMS5599
21. E08 Committee, Practice for conducting force controlled constant amplitude axial fatigue tests of metallic materials, ASTM International n.d. https://doi.org/10.1520/E0466-15
22. Teasley T, Gradl P, Tinker D, Mireles O, Diaz A (2022) Component performance and application characteristics. Met Addit Manuf Propuls Appl, American Institute of Aeronautics and Astronautics, Reston, Virginia
23. AMS F Corrosion Heat Resistant Alloys Committee, Heat treatment nickel alloy and cobalt alloy parts, SAE International n.d. https://doi.org/10.4271/AMS2774G
24. ISO E (1997) 4287:1997 Geometrical product specifications (GPS) – surface texture: profile method – terms, definitions and surface texture parameters, International Organization for Standardization, 2015.
25. Patterson AL (1939) The Scherrer formula for X-ray particle size determination. Phys Rev 56:978–982. https://doi.org/10.1103/PhysRev.56.978
26. Rai SK, Kumar A, Shankar V, Jayakumar T, Bhanu Sankara Rao K, Raj B (2004) Characterization of microstructures in Inconel 625 using X-ray diffraction peak broadening and lattice parameter measurements. Scr Mater 51:59–63. https://doi.org/10.1016/j.scriptamat.2004.03.017

27. Cabrini M, Lorenzi S, Testa C, Pastore T, Brevi F, Biamino S, Fino P, Manfredi D, Marchese G, Calignano F, Scenini F (2019) Evaluation of corrosion resistance of Alloy 625 obtained by laser powder bed fusion. J Electrochem Soc 166:C3399–C3408. https://doi.org/10.1149/2.0471911jes
28. Brytan Z (2016) The passivation treatment of stainless steel surface studied by electrochemical impedance spectroscopy. Jeju Island, Korea
29. Leban MB, Mikyška Č, Kosec T, Markoli B, Kovač J (2014) The effect of surface roughness on the corrosion properties of type AISI 304 stainless steel in diluted NaCl and urban rain solution. J Mater Eng Perform 23:1695–1702. https://doi.org/10.1007/s11665-014-0940-9
30. Yan X, Gao S, Chang C, Huang J, Khanlari K, Dong D, Ma W, Fenineche N, Liao H, Liu M (2021) Effect of building directions on the surface roughness, microstructure, and tribological properties of selective laser melted Inconel 625. J Mater Process Technol 288:116878. https://doi.org/10.1016/j.jmatprotec.2020.116878
31. Yasa E, Kruth J (2011) Application of laser re-melting on selective laser melting parts. Adv Prod Eng Manag 6:259–270
32. Ye C, Zhang C, Zhao J, Dong Y (2021) Effects of post-processing on the surface finish, porosity, residual stresses, and fatigue performance of additive manufactured metals: a review. J Mater Eng Perform 30:6407–6425. https://doi.org/10.1007/s11665-021-06021-7
33. Shankar V, Rao BS, Mannan SL (2001) Microstructure and mechanical properties of Inconel 625 superalloy. J Nucl Mater 288:222–232
34. Marchese G, Lorusso M, Parizia S, Bassini E, Lee J-W, Calignano F, Manfredi D, Terner M, Hong H-U, Ugues D, Lombardi M, Biamino S (2018) Influence of heat treatments on microstructure evolution and mechanical properties of Inconel 625 processed by laser powder bed fusion. Mater Sci Eng A 729:64–75. https://doi.org/10.1016/j.msea.2018.05.044
35. Prochaska S, Hildreth O (2022) Effect of chemically accelerated vibratory finishing on the corrosion behavior of laser powder bed fusion 316 L stainless steel. J Mater Process Technol 117596. https://doi.org/10.1016/j.jmatprotec.2022.117596
36. Gao Y, Ding Y, Ma Y, Chen J, Wang X, Xu J (2022) Evolution of annealing twins in Inconel 625 alloy during tensile loading. Mater Sci Eng A 831:142188. https://doi.org/10.1016/j.msea.2021.142188
37. Wang W, Lartigue-Korinek S, Brisset F, Helbert AL, Bourgon J, Baudin T (2015) Formation of annealing twins during primary recrystallization of two low stacking fault energy Ni-based alloys. J Mater Sci 50:2167–2177. https://doi.org/10.1007/s10853-014-8780-4
38. Barr CM, Vetterick GA, Unocic KA, Hattar K, Bai X-M, Taheri ML (2014) Anisotropic radiation-induced segregation in 316L austenitic stainless steel with grain boundary character. Acta Mater 67:145–155. https://doi.org/10.1016/j.actamat.2013.11.060
39. Hu C, Xia S, Li H, Liu T, Zhou B, Chen W, Wang N (2011) Improving the intergranular corrosion resistance of 304 stainless steel by grain boundary network control. Corros Sci 53:1880–1886. https://doi.org/10.1016/j.corsci.2011.02.005
40. Hyer H, Newell R, Matejczyk D, Hsie S, Anthony M, Zhou L, Kammerer C, Sohn Y (2021) Microstructural development in as built and heat treated IN625 component additively manufactured by laser powder bed fusion. J Phase Equilibria Diffus 42:14–27. https://doi.org/10.1007/s11669-020-00855-9
41. Dubiel B, Sieniawski J (2019) Precipitates in additively manufactured Inconel 625 superalloy. Materials 12:1144. https://doi.org/10.3390/ma12071144
42. Advani AH, Murr LE, Atteridge DG, Chelakara R, Bruemmer SM (1991) Deformation effects on intragranular carbide precipitation and transgranular chromium depletion in type 316 stainless steels. Corrosion 47:939–947. https://doi.org/10.5006/1.3585206
43. Godec M, Skobir Balantič DA (2016) Coarsening behaviour of M23C6 carbides in creep-resistant steel exposed to high temperatures. Sci Rep 6:29734. https://doi.org/10.1038/srep29734
44. De Terris T, Castelnau O, Hadjem-Hamouche Z, Haddadi H, Michel V, Peyre P (2021) Analysis of as-built microstructures and recrystallization phenomena on Inconel 625 alloy obtained via laser powder bed fusion (L-PBF). Metals 11:619. https://doi.org/10.3390/met11040619
45. de Leon Nope G, Wang G, Alvarado-Orozco JM, Gleeson B (2022) Role of elemental segregation on the oxidation behavior of additively manufactured Alloy 625. J Miner Met Mater Soc. https://doi.org/10.1007/s11837-022-05200-8
46. Smith G, Eisinger N (2004) The effect of niobium on the corrosion resistance of nickel-base alloys. Int Symp Niobium High Temp Appl TMS (The Minerals, Metals & Materials Society) pp. 23–34
47. Ha H-Y, Lee T-H, Bae J-H, Chun D (2018) Molybdenum effects on pitting corrosion resistance of FeCrMnMoNC austenitic stainless steels. Metals 8:653. https://doi.org/10.3390/met8080653
48. Cabrini M, Lorenzi S, Testa C, Brevi F, Biamino S, Fino P, Manfredi D, Marchese G, Calignano F, Pastore T (2019) Microstructure and selective corrosion of Alloy 625 obtained by means of laser powder bed fusion. Materials 12:1742. https://doi.org/10.3390/ma12111742
49. Fredriksson W, Petrini D, Edström K, Björefors F, Nyholm L (2013) Corrosion resistances and passivation of powder metallurgical and conventionally cast 316L and 2205 stainless steels. Corros Sci 67:268–280. https://doi.org/10.1016/j.corsci.2012.10.021
50. Vernouillet A, Put AV, Pugliara A, Doublet S, Monceau D (2020) Monceau, Metal dusting of Inconel 625 obtained by laser beam melting: effect of manufacturing process and hot isostatic pressure treatment. Corros Sci 174(2020):108820. https://doi.org/10.1016/j.corsci.2020.108820
51. Seifert M, Huth S, Siebert S, Theisen W (2015) Wear- and corrosion-resistant steels containing niobium carbide. Int Symp Wear Resist Alloys Min Process Ind. CBMM, São Paulo, Brazil, pp 197–221
52. Wu LH, Jiang CH (2017) Effect of shot peening on residual stress and microstructure in the deformed layer of Inconel 625. Mater Trans 58:164–166. https://doi.org/10.2320/matertrans.M2016298
53. Bilgili AK, Çağatay R, Dervişoğlu HC, Öztürk MK (2021) Determination of dislocation density and correlation length of Si, Ti, Au and Zno on Ge by peak profile. Review. https://doi.org/10.21203/rs.3.rs-216388/v1
54. Moram MA, Vickers ME (2009) X-ray diffraction of III-nitrides. Rep Prog Phys 72